Article

Multiphasic Coacervates Assembled by Hydrogen Bonding and Hydrophobic Interactions

Xinhao Liu, Abdol Hadi Mokarizadeh, Amal Narayanan, Prathamesh Mane, Avanti Pandit, Yen-Ming Tseng, Mesfin Tsige, and Abraham Joy*
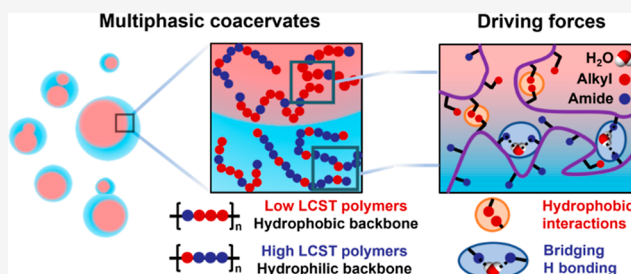
Read Online

ACCESS | Metrics & More | Article Recommendations | SI Supporting Information

ABSTRACT: Coacervation has emerged as a prevalent mechanism to compartmentalize biomolecules in living cells. Synthetic coacervates help in understanding the assembly process and mimic the functions of biological coacervates as simplified artificial systems. Though the molecular mechanism and mesoscopic properties of coacervates formed from charged coacervates have been well investigated, the details of the assembly and stabilization of nonionic coacervates remain largely unknown. Here, we describe a library of coacervate-forming polyesteramides and show that the water-tertiary amide bridging hydrogen bonds and hydrophobic interactions stabilize these nonionic, single-component coacervates. Analogous to intracellular biological coacervates, these coacervates exhibit "liquid-like" features with low viscosity and low interfacial energy, and form coacervates with as few as five repeating units. By controlling the temperature and engineering the molar ratio between hydrophobic interaction sites and bridging hydrogen bonding sites, we demonstrate the tuneability of the viscosity and interfacial tension of polyesteramide-based coacervates. Taking advantage of the differences in the mesoscopic properties of these nonionic coacervates, we engineered multiphasic coacervates with core−shell architectures similar to those of intracellular biological coacervates, such as nucleoli and stress granule-p-body complexes. The multiphasic structures produced from these synthetic nonionic polyesteramide coacervates may serve as a valuable tool for investigating physicochemical principles deployed by living cells to spatiotemporally control cargo partitioning, biochemical reaction rates, and interorganellar signal transport.

INTRODUCTION

Coacervation is the liquid−liquid phase separation (LLPS) of a homogeneous polymer solution into two immiscible liquid phases: a polymer-concentrated phase (dense phase) and a polymer-depleted phase (dilute phase). The dense phase, commonly termed coacervate, is a weakly associated network percolated with hydrophobic interactions, hydrogen bonding (HB), and electrostatic interactions.[1−3] The "liquid-like" behavior of coacervates is extensively used by nature to control and organize biological processes such as cellular compartmentalization, extracellular matrix formation, cell replication, and organismal underwater adhesion.[4] For example, sandcastle worms and mussels secrete coacervate-forming adhesive proteins to achieve strong interfacial adhesion on underwater surfaces.[5−7] Delivery of polymer-concentrated coacervates minimizes loss of the polymer into the seawater and facilitates adhesion, positioning, and spreading at the desired underwater site.[8]

In living cells, coacervation has been proposed as a strategy to spatially organize and sequentially regulate biochemical activities in membraneless organelles including nucleoli, stress granules, and nuclear speckles.[9] In the absence of a confining membrane, living systems mus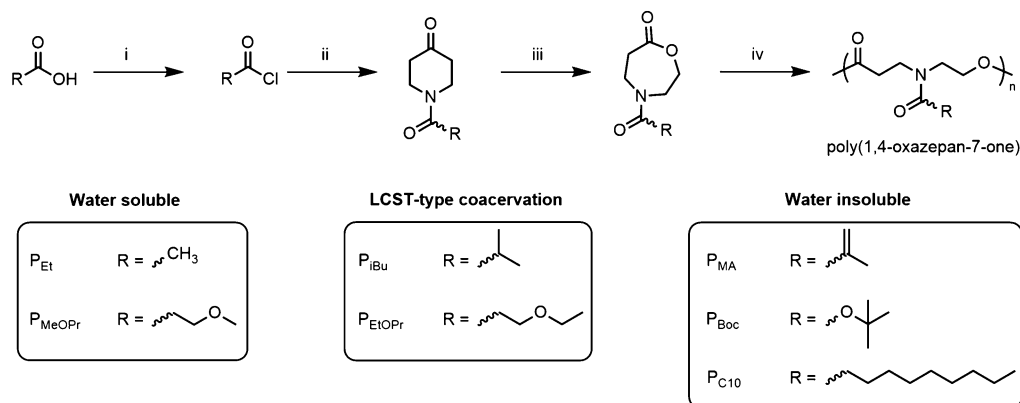t use a plethora of nucleic acid and protein chemistries in membraneless organelles to perform spatiotemporally regulated biochemical reactions. The prerequisite of cellular homeostasis while regulating crucial biochemical reactions often necessitates highly complex protein and nucleic acid chemistries—making the characterization of the underlying molecular details in membraneless organelles rather challenging. Therefore, simple systems that replicate the structural and molecular diversity of coacervating biomacromolecules in living systems are required for the exploration of underlying coacervation mechanisms and for making functional mimetics of complex membraneless organelles.[9]

Advances in molecular biology techniques have enabled the creation of biological coacervates that can be formed, altered, or disrupted through engineering molecular interactions by altering the amino acid sequence,[10−13] charge density,[12,14−16]

Scheme 1. Synthesis Scheme of *N*-Functional Poly(1,4-oxazepan-7-one)s (P$_x$, where the Subscript *x* Denotes the Side Group)^a

^{a}Steps: (i) synthesis of acyl chlorides (conditions: thionyl chloride, 0 °C to R.T., 6 h), (ii) amidation reaction (conditions: 4-piperidone hydrochloride monohydrate, potassium carbonate, dichloromethane, R.T., 24 h), (iii) Baeyer–Villiger oxidation (conditions: 3-chloroperoxybenzoic acid, dichloromethane, R.T., 24 h), and (iv) ROP (conditions: triazabicyclodecene, dichloromethane, benzyl alcohol, R.T., 10 min).

hydrophobicity,[17,18] and oligomerization[19−21] of biomacromolecules.[22−25] An alternative strategy to investigate the mesoscopic properties of biological coacervates is to use synthetic coacervates as a simplified model. In recent years, the materials family for such model coacervates has expanded from proteins and nucleic acids to synthetic polyacrylates,[26] polyesters,[8,27−29] and peptides.[16] However, most of these synthetic coacervates are classically prepared from oppositely charged polymers, which can be unstable at high ionic strength and at extreme pH ranges.[11,30,31] While there have been reports on single-component coacervation of proteins,[7] nucleic acids,[32] and synthetic polymers,[33,34] the progress toward a molecular-level understanding of how phase behavior is encoded in the chemical structure is limited compared to charged polymer coacervates. Therefore, there is a need for a simple single-component system with an atomistic resolution of the origin of coacervation and tuneable phase behavior to engineer charge-free "nucleoli-like" functional multiphasic coacervates.

Previously our laboratory had reported a library of coacervate-forming, nonionic polyesteramides synthesized via step-growth polymerization of diacids and *N*-functionalized diols.[28,29,35] Though the step-growth polymerization used for their synthesis offers easy preparation and scalability, the synthesis method has poor control over the monomer distribution, end group functionality, and molar mass (M_n). These shortcomings hamper an in-depth study of the phase behavior and structure−property relationship of polyesteramide coacervates.[34,36] ROP-derived polyesteramides have superior control over M_n, narrow M_n distribution, and a better handle on the polymer architecture. Herein, we prepared nonionic coacervate-forming polyesteramides using ring-opening polymerization (ROP) of *N*-acylated-1,4-oxazepan-7-ones with a diversity of side-chain chemistries. Indeed, we found that some of the ROP-derived polyesteramides demonstrated lower critical solution temperature (LCST)-type coacervation, where they are miscible with water at low temperatures and phase separate into two liquid phases at a higher temperature. Oftentimes, LCST is thought to be driven by hydrophobic interactions, as demonstrated for poly(*N*-isopropylacrylamide) (PNIPAM) and poly(2-isopropyl oxazoline).[37,38] However, based on the tailored molecular structure, temperature-

dependent Fourier transformation infrared (FTIR) spectroscopy, and atomistic molecular dynamics (MD) simulation of the polyesteramides, we found that in addition to hydrophobic interactions, water-bridged HB acts as a catalyst for the coacervation. By comparing polyesteramides with identical side groups but different backbone chemistries, we also show that the phase behavior of coacervates can be tuned by the temperature and the ratio of hydrophobic to water-bridged HB sites. The coacervates made from polyesteramides in water showed low viscosity and low interfacial tension. Similar to biological coacervates, these polyesteramide coacervates form multiphasic coacervates when coacervates with distinct interfacial tensions are mixed. We propose that these polyesteramide coacervates with atomistic precision on material properties and phase behavior are a simple model that can reconstitute the mesoscopic properties and physiological functions of biomolecular coacervates.

■ RESULTS AND DISCUSSION

Design and Synthesis of Polyesteramides Using ROP. Synthetic coacervates, inspired by biological coacervates, are typically made from polypeptides[22,34,39,40] and polyacrylates.[30,41−43] Polyesteramides[44] are excellent analogues of polypeptides for creating synthetic coacervates because of their scalability, potential for biorecognition,[45,46] hydrolytic degradability,[47] and broad availability of *N*-substituted side-group chemistries, including peptide-like pendent groups.[48,49] Previously, Swanson et al. reported coacervation behavior in polyesteramides synthesized from step-growth polyesterifications between *N*-functionalized diethanolamides and linear dicarboxylic acids.[28,29] In aqueous media, a large library of these polyesteramides showed LCST behavior, and above their respective critical temperature, the homogeneous polyesteramide solutions displayed LLPS to form dense and dilute phases.[8] However, the step-growth polymerization method has minimal control over the M_n and forms polymers with broad M_n distributions (polydispersity = 1.6−2.3),[50,51] which makes it challenging to determine the molecular parameters for coacervation.

The ROP of 1,4-oxazepan-7-ones (OxP) developed by Wang[52] offers an alternative to the polyesteramide synthesis with controlled M_n and M_n distribution. The OxP monomers
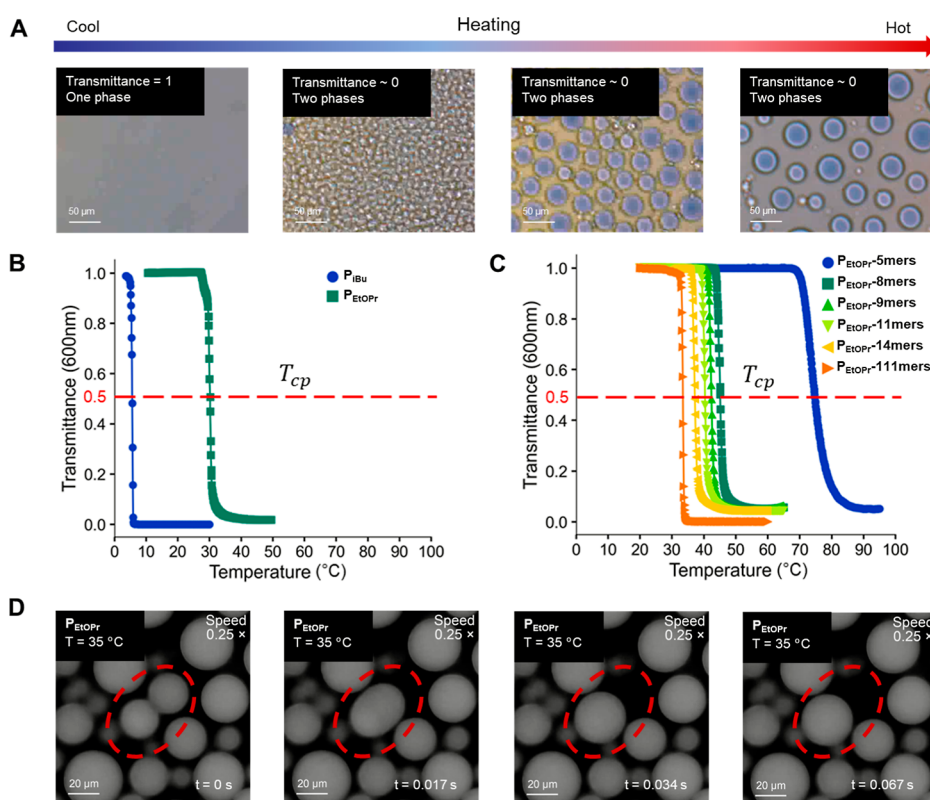
Figure 1. (A) Representative microscopic visualization of the LCST behavior of P_{EtOPr} (M_n = 24 kDa) and its corresponding transmittance (measured from turbidimetry at 600 nm). With the increase of temperature above 26 °C, the clear solution turns turbid, accompanied by the formation and growth of immiscible microdroplets. (B) LCST behavior of P_{iBu} (M_n = 13 kDa) and P_{EtOPr} (M_n = 24 kDa) in DI water. Turbidity was determined for individual polymer solutions at a concentration of 10 mg/mL from transmittance measurements at 600 nm using UV−vis spectroscopy. The cloud point temperature (T_{cp}) was determined as the temperature at 50% transmittance, as denoted by the red dashed line. (C) LCST behavior of P_{EtOPr} polymers with a varying number of repeating units (number of repeating units = 5, 8, 9, 11, 14, and 111) in DI water. Similar protocols to those in Figure 1B were followed for turbidity measurements and T_{cp} determination. (D) Coalescence event of rhodamine B-conjugated P_{EtOPr} droplets (M_n = 24 kDa, concentration = 10 mg/mL) was observed with fluorescence microscopy at 35 °C. The time (t) on the bottom right of each image indicates the actual time in the original videos (1× playing speed). The dashed red circle highlights the droplets in coalescence (see Video S2).

were obtained by (i) preparation of the acyl chloride, (ii) amidation of 4-piperidone with the acyl chloride, and (iii) ring expansion by Baeyer−Villiger oxidation (Scheme 1). The ROP of the OxPs was performed with an organocatalyst (triazabicyclodecene) at room temperature (Scheme 1, see the Supporting Information for details). We developed OxP homopolymers (P_x) with various groups, such as 3-ethoxypropyl (EtOPr), 3-methoxypropyl (MeOPr), and isobutyl (iBu). The subscript x of P_x indicates the side group of the polyesteramide homopolymers. For example, P_{EtOPr} represents poly(1,4-oxazepan-7-one) with a 3-ethoxypropyl pendent group. The synthetic scheme and procedures are shown in Scheme 1 and in the Supporting Information. Polymers with well-documented LCST behavior such as PNIPAM,[53] oligo(ethylene glycol) functionalized polyacrylates (POEG),[54] and polyoxazolines[55] inspired the design of polymers with isobutyl (P_{iBu}, PNIPAM-like) and ethoxypropyl (P_{EtOPr}, POEG-like) pendant functional groups.

Determination of LCST-Type Coacervation of Polyesteramides in Water. Turbidity measurements in deionized (DI) water across 0−100 °C were used to determine the phase separation behavior of the polyesteramides. The polymers P_{Et} and P_{MeOPr} were fully soluble in water, whereas P_{MA}, P_{Boc}, and P_{C10} were insoluble in water in the temperature and concentration ranges tested. Interestingly, both P_{iBu} and P_{EtOPr}

were soluble in water at lower temperatures (<4 °C for P_{iBu} and <26 °C for P_{EtOPr}) and showed an LCST-type phase transition at higher temperatures (Figure 1B). The turbidity measurements were followed with fluorescence microscopy to evaluate the coacervate behavior of the turbid phase above the LCST. We found that both polymers formed microscopic droplets (Figure 1A). Upon contact with each other, these droplets coalesced and relaxed into a spherical shape to minimize their surface tension. The coalescence of two dense phase microdroplets was completed within one second for both P_{iBu} and P_{EtOPr} (Figure 1D, Video S1, Video S2). The ability of dense phases to fuse and coalesce confirms their liquid-like behavior and their ability to undergo LLPS in water above LCST.[34,56−58]

Coacervation has been reported to be driven by HB, hydrophobic interactions, cation−pi, and pi−pi interactions.[59] Here, we investigated the driving forces that determine the coacervation of polyesteramides by FTIR and simulation. P_{EtOPr} was chosen as a representative example because of its accessible phase-transition temperature (T_{cp} of P_{EtOPr} = 30.2 °C, M_n = 24 kDa). To simplify the system and minimize the effect of end groups on coacervation, we examined the dependence of the chain length on the T_{cp}. We took advantage of ROP for the excellent control of the M_n of the polyesteramides and examined the dependence of the T_{cp} on
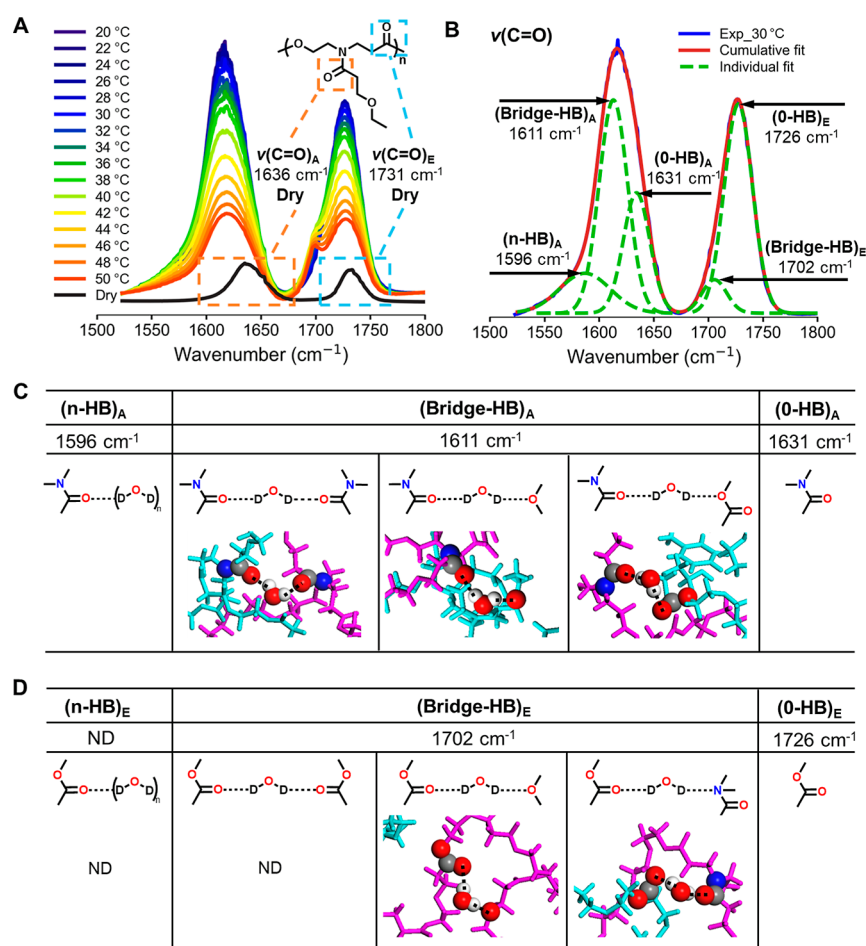
Figure 2. Temperature-dependent FTIR spectra of P_{EtOPr}. (A) Baseline-subtracted $\nu(C=O)$ bands of P_{EtOPr} (10 wt % in D_2O) at 20−50 °C and as a dry solid P_{EtOPr} at 20 °C. (B) $\nu(C=O)$ bands (solid lines) and sub-bands (broken lines) of P_{EtOPr} (10 wt % in D_2O) at 30 °C. Each sub-band is assigned as follows: 1596 cm^{-1} for $(n\text{-HB})_A$, 1611 cm^{-1} for $(bridge\text{-HB})_A$, 1631 cm^{-1} for $(0\text{-HB})_A$, 1702 cm^{-1} for $(bridge\text{-HB})_E$, and 1726 cm^{-1} for $(0\text{-HB})_E$. (C) Visualization of all $\nu(C=O)_A$ and zoomed-in snapshots of $(bridge\text{-HB})_A$ presented in the final configuration (time = 180 ns) of polymer chains in the water system at 360 K from atomistic MD simulations (oxygen atoms: red spheres; hydrogen atoms: white spheres; and polymer chains: red, purple, and cyan sticks and lines). (D) Visualization of $\nu(C=O)_E$ and zoomed-in snapshots of $(bridge\text{-HB})_E$ are presented in the same MD simulation as that in Figure 2C. ND: not detected in the system.

the chain length of P_{EtOPr}. Here, by controlling the feed ratio of the monomer to the initiator, P_{EtOPr} with 5−111 repeating units were prepared. The number of monomers per chain was characterized by the ratio of characteristic ^1H NMR peak areas (Figure S1). Notably, we observed an abrupt increase in the T_{cp} as the number of repeating units decreased below 8. This behavior may be originating from the dominance of polymer end group-driven interactions and switching between intermolecular (e.g., polymer chain A with polymer chain B) interactions to intramolecular interactions at smaller chain lengths. For the FTIR study, we chose P_{EtOPr} with 111 repeating units (M_n = 24 kDa) due to its accessible T_{cp}. A small shift of T_{cp} from 14 to 111 repeating units allows us to use P_{EtOPr} with 14 monomers as a minimal system in the simulation to capture the behavior of P_{EtOPr} with longer chains under experimental conditions. Note that P_{EtOPr} can exhibit LLPS behavior down to about five repeating units, $M_n \sim 1.1$ kDa (Figure 1C)—making it one of the smallest molecules with LLPS behavior.[22,34,60−62]

Characterization of the Driving Forces for the Coacervation of Polyesteramides. Temperature-dependent FTIR spectra of 10 wt % P_{EtOPr} (M_n = 24 kDa) in D_2O were collected to investigate the driving forces of the

coacervation.[10,39,63] The spectra were collected at temperatures from 20 to 50 °C with a step interval of 2 °C. Also, D_2O was used instead of H_2O to eliminate the FTIR spectral overlap of the $\delta(OH)$ band of water at ~1640 cm^{-1} with the $\nu(C=O)$ bands from the polyesteramide backbone. The $\nu(C=O)$ bands from 1525 to 1800 cm^{-1} that probe carbonyl groups from both tertiary amide ($\nu(C=O)_A$) and ester ($\nu(C=O)_E$) functional groups of the polyesteramides (Figure 2A) were used for a detailed analysis. The $\nu(C=O)$ region (1525 to 1800 cm^{-1}) is populated with several IR stretching modes such as $(0\text{-HB})_A$, $(bridge\text{-HB})_A$, $(n\text{-HB})_A$, $(0\text{-HB})_E$, $(bridge\text{-HB})_E$, and $(n\text{-HB})_E$. 0-HB represents carbonyls with no HB, whereas n-HB denotes carbonyls HB with one or more water molecules and bridge-HB represents carbonyls HB with another HB site through water bridges (Figure 2C). The subscripts A and E represent C=O from amides and esters, respectively. We deconvoluted the carbonyl region with Gaussian fitting[64] to assign each stretching mode.

Figure 2B shows the dissection and peak assignment of the crowded $\nu(C=O)$ region at 30 °C with the best fitting ($R^2 > 0.995$). For P_{EtOPr} in D_2O at 30 °C, the $\nu(C=O)_A$ bands were fitted with three sub-bands centered around 1596, 1611, and 1631 cm^{-1}. Because the $\nu(C=O)_A$ band of dry solid P_{EtOPr}
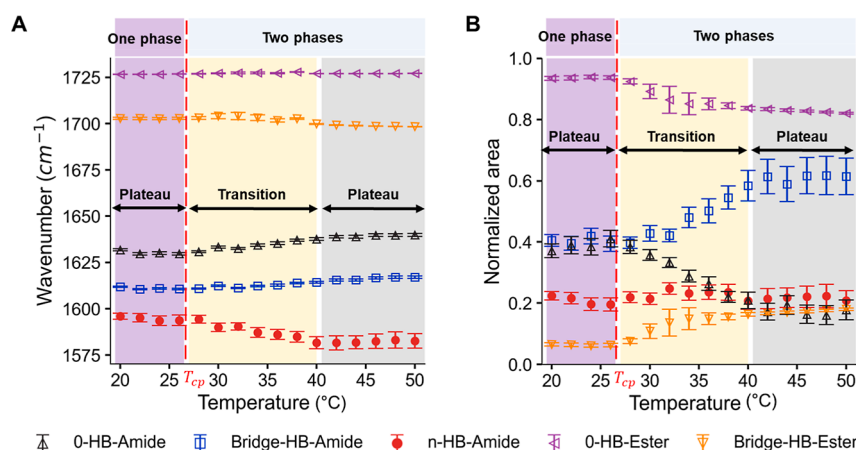
Figure 3. Temperature-dependent shift of (A) wavenumber maxima of $\nu(C=O)$ sub-bands. (B) Normalized area (A %) of $\nu(C=O)$ sub-bands. The area of each C=O is normalized to the total area of the C=O of tertiary amides or esters. For example, A % of $\nu(C=O\cdots D-O-D)_A$ is equal to the area of $\nu(C=O\cdots D-O-D)_A$ divided by the total area of $\nu(C=O)_A$. The vertical red dashed line indicates the T_{cp} of P_{EtOPr} in D_2O. Three distinct regions: an initial plateau, a transition region, and a second plateau are observed in $\nu(C=O)$ sub-bands that were affected by coacervation.

with no HB (there are no HB donors in dry conditions) was observed at 1635 cm^{-1}, the sub-band in the spectra of polyesteramide solutions at 1631 cm^{-1} was assigned to $(0\text{-HB})_A$ (amide carbonyl with no HB). Atomistic MD simulation of 10 chains of P_{EtOPr} (number of repeating units = 14) in 20,000 water molecules showed the presence of $(0\text{-HB})_A$, $(\text{bridge-HB})_A$, and $(n\text{-HB})_A$ in the system (Figure 2C). Additionally, at all temperatures, the average O$\cdots$H distance of $(\text{bridge-HB})_A$ is shorter than that of $(n\text{-HB})_A$ (Figure S2). Therefore, the carbonyl of $(\text{bridge-HB})_A$ has a less double bond nature, lower bond strength, and higher wavenumber than that of $(n\text{-HB})_A$. Based on the MD simulation results, the sub-bands 1611 and 1596 cm^{-1} were assigned to $(\text{bridge-HB})_A$ and $(n\text{-HB})_A$, respectively. Similarly, the ester carbonyl $\nu(C=O)_E$ bands were fitted with two sub-bands that peak at 1726 and 1702 cm^{-1}, and these were assigned to $(0\text{-HB})_E$ and $(\text{bridge-HB})_E$, respectively (Figure 2D). The descending order of amide peak positions: $(0\text{-HB})_A$ (1631 cm^{-1}) > $(\text{bridge-HB})_A$ (1611 cm^{-1}) > $(n\text{-HB})_A$ (1596 cm^{-1}) observed for P_{EtOPr} followed the same trend as previously reported studies on poly(2-isopropyl-2-oxazoline).[38,65] The absence of $(n\text{-HB})_E$ in MD simulations and the relatively smaller area of $(\text{bridge-HB})_E$ in the total area of esters in $\nu(C=O)_E$ in FTIR indicate that ester groups are weaker HB acceptors than tertiary amides in our polyesteramides. The excellent HB nature of tertiary amides is also confirmed by MD simulations, which show that the majority of bridge-HB is contributed by tertiary amides over esters and ethers. The number of bridge-HB between tertiary amides is three times that of esters and ethers (Figure S3).

To provide a quantitative framework for the molecular origin of the LLPS of P_{EtOPr}, the temperature-dependent shift of the $\nu(C=O)$ peaks and the normalized area of the deconvoluted carbonyl bands were determined (Figure 3). With the increase in temperature, the wavenumber and the normalized area of all carbonyl groups in P_{EtOPr} show three distinct regions: (i) an initial plateau region (<27 °C), (ii) a broad transition region at the onset of LCST (27−40 °C), and (iii) a second plateau (>40 °C). The onset of LCST of PNIPAM has previously been reported as a relatively sharp transition (32−37 °C).[37,66] Okada and Tanaka suggested that the presence of the hydrophobic isopropyl group hinders HB

between water and secondary amides on PNIPAM.[67] Also, the water in the polymer hydration layer of PNIPAM is energetically favored to form hydrogen bonds with neighboring water to establish a highly cooperative water network. Upon temperature elevation above LCST, PNIPAM loses the strongly cooperative water network surrounding the polymer chains and forms intramolecular hydrogen bonds between secondary amide groups.[37,67] In Okada's model, the transition becomes sharper with an increase in water cooperativity. Unlike PNIPAM, tertiary amides in P_{EtOPr} are not sterically hindered by hydrophobic groups and are free to form hydrogen bonds with water. This competes with water−water HB, disrupts the cooperativity of the hydration layer, and forms a weakly coordinated network. The broad LCST transition of P_{EtOPr} originates from the relatively slow dehydration of weakly coordinated hydration layer and weak polymer−polymer interactions.

As the temperature increases, the $(n\text{-HB})_A$ shifts to lower wavenumbers while the $(0\text{-HB})_A$ and $(\text{bridge-HB})_A$ shift to higher wavenumbers (Figure 3A). The shift in carbonyl peak positions during heating is an indication of changes in hydration degree and chain conformation of polymers with LCST.[37,68] One possible scenario for this behavior is that $(n\text{-HB})_A$ becomes more hydrated to stabilize the dehydrating $(0\text{-HB})_A$ and $(\text{bridge-HB})_A$ and prevent the precipitation of polymers. Notably, we observed that the normalized area of $(\text{bridge-HB})_A$ increased while the normalized area of $(0\text{-HB})_A$ decreased (Figure 3B), indicating that during the heating process, $(0\text{-HB})_A$ gradually transforms into $(\text{bridge-HB})_A$. Therefore, bridge-HB serves to stabilize the weakly associated polymer−water network, which is a visualization of the coacervate microstructure. Compared to the amide functional groups, the ester groups in the polyesteramide backbones undergo a slightly different process during the phase separation. We observed that the percentage of the $(\text{bridge-HB})_E$ population grows (Figure 3B) but the $(\text{bridge-HB})_E$ becomes more hydrated (Figure 3A). This can be attributed to the poor hydration of esters at temperatures below the LCST. During heating, some of the $(0\text{-HB})_A$ transitions to $(\text{bridge-HB})_A$ by moving to the polymer−water interface from the hydrophobic region along polymer chains. During heating, $\nu(C-H)$ sub-bands (Figures S4 and S5) blue-shifted,

indicating the dehydration of alkyl groups. Together with the dehydration (red-shift in FTIR) of $(0\text{-HB})_A$ and $(\text{bridge-HB})_A$ amides, hydrophobic interactions also serve as the driving force for LLPS.

Coacervate Structure-Mesoscopic Physical Property Relationships. After confirming the role of bridging HB and hydrophobic interactions in driving the coacervation of polyesteramides, next we investigated the structure–property relationship of this multi-interaction-driven coacervation. Here, C2−E0, C4−E1, and C6−E2 polymers with the same M_n were synthesized using cationic polymerization, ROP, and step-growth polymerization, respectively (Table 1 and Scheme S1).
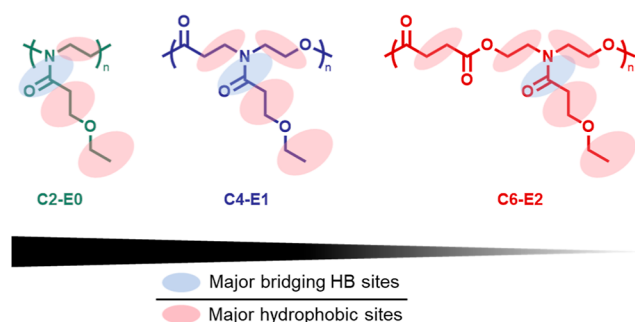
Table 1. Summary of the Molecular Characterization of Three Thermoresponsive Coacervate-Forming Polymers, C2−E0, C4−E1, and C6−E2

polymer	LCST^a (°C)	$T_{cp}{}^b$ (°C)	M_n (kDa)	Đ	Tg (°C)
C2−E0	51.3	54.2	24.2	1.27	8.0
C4−E1	26.2	30.2	24.1	1.30	−11.5
C6−E2	1.8	6.2	23.8	1.85	−11.9

^{a}LCST is approximated by best fitting with the Iring equation.[69] $^bT_{cp}$ is determined by cloud point measurements.

The polymer nomenclature C*m*−E*n* in Scheme 2 describes that there are *m* alkyl groups and *n* esters in the backbone of

Scheme 2. Chemical Structures of C2−E0, C4−E1, and C6−E2 Polymers for Investigating the Structure−Property Relationship of Multiple Interaction-Driven Coacervates^a

^{a}Three polymers have identical M_n and share the same side group. The ratio of major bridging HB sites and major hydrophobic sites decreases in the following order: C2−E0 > C4−E1 > C6−E2. Major bridging HB sites (blue ellipse): tertiary amides. Major hydrophobic sites (red ellipse): alkyl groups. Minor HB site and minor hydrophobic sites: esters and ethers based on FTIR and atomistic MD simulation results.

each repeating unit. These polymers share the same 3-ethoxypropanoyl amide (EtOPr) side group but vary in the numbers of alkyl and ester groups in the backbone of the repeating unit. Note that C4−E1 has the same polymer structure as P_{EtOPr}. Further discussion will use C4−E1 instead of P_{EtOPr} to emphasize the differences in backbones among polyesteramides. According to our FTIR studies and atomistic MD simulations, the alkyl groups are defined as major hydrophobic groups and tertiary amides are major HB sites, and hence, they contribute to hydrophobic interactions and bridging HB, respectively. At the same M_n, the ratio of bridging HB sites and hydrophobic sites should follow the order depicted in Scheme 2, which allows us to correlate the

interplay of bridging HB and hydrophobic interactions on the properties of the coacervates.

First, the LLPS nature of the three polymers was confirmed by turbidity measurements and coalescence experiments (Videos S2, S3 and S4). The phase diagrams of three polymers were constructed to visualize the coacervate compositional response to temperature (Figure 4A for a representative LCST-type phase diagram). The compositional measurements (wt %) were obtained by gravimetric analysis of the solid content of the dilute and dense phases after lyophilization (see the Supporting Information for details). The phase diagram visualizes the boundary between the upper (dense phase) and the lower (dilute phase) phases. From C2−E0 to C6−E2, the two-phase window of the coacervates is broadened and shifted to a lower temperature (Figure 4B). The LCST of the polymer in aqueous media decreases in the following order: C2−E0 > C4−E1 > C6−E2 (Table 1). This follows the same trend observed in other LCST-type coacervate systems,[29,42,70] in which the increase in hydrophobicity causes the temperature depression of the phase boundary. To further understand the binodal curve, the phase diagram was subjected to binodal curve fitting derived from the simplified Flory−Huggins theory (see the Supporting Information for details). This model has been found to describe the critical salt concentration and experimental phase behavior of coacervates with corrected interaction parameters that account for the electrostatic interactions.[11,15,71] However, a notable discrepancy was observed for the Flory−Huggins-model-based binodal curve fitting for C4−E1 and C6−E2. The inaccurate fitting potentially stems from HB and other electrostatic interactions, which are not addressed by the simplified Flory−Huggins model. The cause of the discrepancy can also be due to the potential errors in the obtained concentrations of the dilute phase due to the limitations for accurate gravimetric analysis of the solid content at low polymer concentrations.

In living cells, it is hypothesized that modulating the viscosity of coacervates offers a pathway to control the influx and outflux of guest molecules for responding to environmental stress.[72] Typically, the viscosity of biological coacervates varies between 0.01 and 50 Pa·s as measured from fluorescence recovery photobleaching[57,73] and microrheology[74,75] experiments. Here, we used particle tracking microrheology[76] to estimate the viscosity of the synthetic coacervates in situ (Figures S8 and S9) and employed them for the interfacial tension calculations. The coacervates made from C2−E0, C4−E1, and C6−E2 polymers showed viscosity in the range of 0.1−10 Pa·s (Figure 5A), which is comparable to biological coacervates and synthetic complex coacervates (0.1−100 Pa·s).[77,78] At 65 °C, the viscosity of the coacervates increased in the following order: C2−E0 (0.0823 Pa·s) < C4−E1 (0.143 Pa·s) < C6−E2 (1.29 Pa·s).

Next, the interfacial tension (γ) was determined for understanding their wetting behavior on polar underwater surfaces, formation of multiphasic coacervate structures, and coacervate Ostwald ripening rate.[3,8,39,58] The interfacial tension refers to the energetic penalty of increasing the interfacial area with units of energy per unit area. Compared to the interfacial tension between pure liquid water and its vapor which is about 72×10^3 μN/m at 25 °C,[79] the interfacial tension between synthetic complex coacervates and the coexisting dilute phase is reported to be around 1−1000 μN/m.[3] For biological coacervates, the interfacial tension varies over several orders of magnitude depending on the
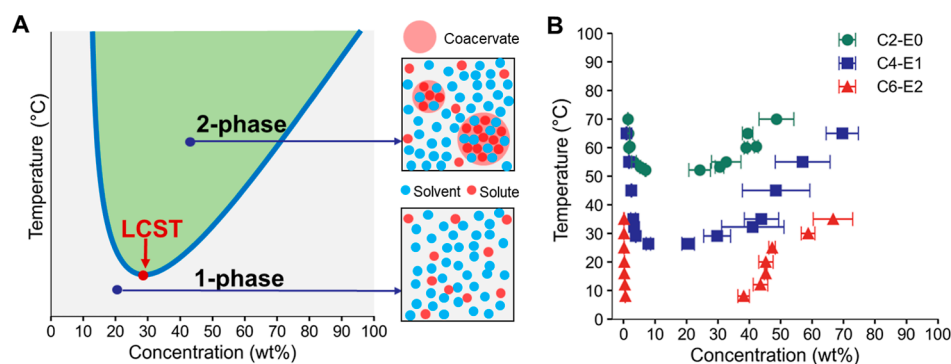
Figure 4. (A) (Left) Model LCST-type phase diagram. (Right) Cartoon representation of the microstructures of one-phase and two-phase regions. (B) Phase diagrams of C2−E0, C4−E1, and C6−E2. Error bars represent the standard deviation of concentrations from three independent measurements.
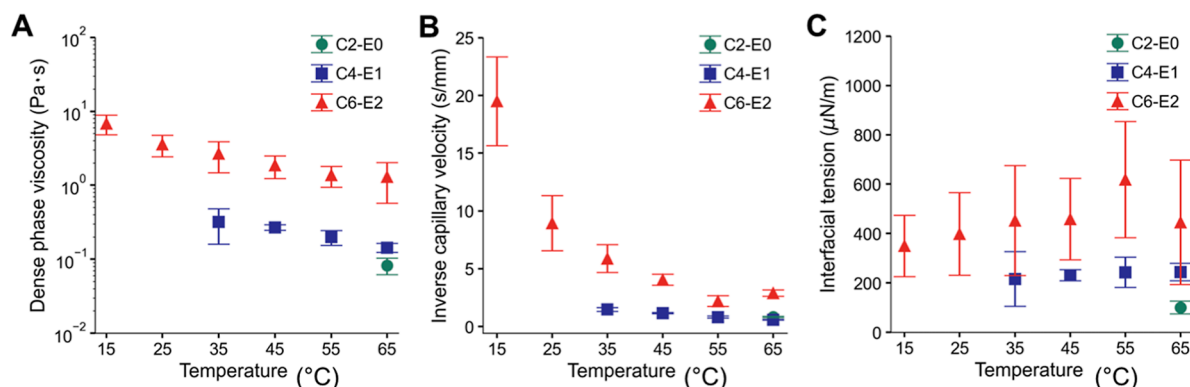

Figure 5. Temperature-dependent changes in the (A) viscosity (η) of the dense phases determined by the microrheology, (B) inverse capillary velocity (η/γ) determined by the coalescence analysis, and (C) interfacial tension calculated from $\eta/(\eta/\gamma)$.

specific constituent macromolecules, ranging from 0.1 to 100 μN/m.[58,74,80] Here, we determined the inverse capillary velocity (η/γ) from the characteristic time of coalescence events (Figures S9, S10 and 5B) and calculated the interfacial tension using the viscosity obtained from microrheology (Figure 5A). The interfacial tension of our synthetic coacervates was determined to be 100−700 μN/m (Figure 5C), which is similar to the values reported for RNA-LAF1 biological coacervates.[74]

Engineering Multiphasic Coacervates Using Interfacial Properties. The multilayered structure of coacervates is a prominent feature among biological coacervates such as nucleoli,[56] stress granule-P-body complexes,[81] and nuclear speckles.[82] The layered compartments within coacervates assist in the spatial control of biological reactions and biomolecular export, as observed in the biogenesis of ribosomes.[83] Several protocells have been shown to mimic dedicated multiphasic structures for cascade enzymatic reactions using synthetic polyelectrolytes.[84,85] A few reports found that the differences in the interfacial tensions between two coacervating polymers in the same solution can drive the formation of multilayered coacervates.[43,58] Here, homogeneous solutions of two polymers with different LCSTs were mixed to form de novo multilayered simple coacervates (Figure 6A−C). For example, C4−E1 (T_{cp} = 30.2 °C) and C2−E0 (T_{cp} = 54.2 °C) were dissolved at 20 °C, and the temperature was increased to 65 °C at a rate of 10 °C/min. Initially, the mixture was homogeneous, and at 65 °C, multiphasic structures started to emerge (Figure 6A). Notably, we observed that the relatively hydrophilic polymer was always concentrated in the shell of a multilayered

structure. The multiphasic structures can emerge as kinetically trapped[14,86,87] and thermodynamically stable systems.[43,88] The kinetically trapped multiphasic systems form upon sudden changes in the composition and become biphasic (dilute and dense phases) with time.[14,86,87] For example, due to a rapid change in the temperature, droplets of the dilute phase can nucleate inside coacervates and coalesce with each other to form kinetically trapped multiphasic structures. Meanwhile, for a thermodynamically stable system, droplets form at a slow change of composition and retain a third distinct phase.[43,88] To test whether multiphasic coacervation is governed by thermodynamics or kinetics, multiphasic coacervates were prepared at a slow heating rate of 3 °C/min. Also, preformed coacervates of C4−E1 (T_{cp} = 30.2 °C) and C2−E0 (T_{cp} = 54.2 °C) were mixed at 65 °C. In our study, all preparation methods produced identical multiphasic droplets, as shown in Figure 6A. Examination of the fluorescence profile of multiphasic droplets in the dilute phase (Figure 6D−H) shows that they have three different compositions. Identical structures by different preparation methods and distinct compositions support that multiphasic droplets are thermodynamically stable multiphasic coacervates.[43]

To understand the formation of core−shell multiphasic coacervates, we examined the spreading coefficients (S_i) of the coacervates, where $S_i = \gamma_{jk} - (\gamma_{ij} + \gamma_{ik})$. The γ_{ij}, γ_{jk}, and γ_{ik} are the interfacial tensions between two liquid phases i and j, j and k, and i and k.[89] These spreading coefficients determine three possible scenarios for the organization of two immiscible droplets, immiscible, partial wetting, and core−shell (complete wetting), as shown in Figure 6D. As an example, we analyzed
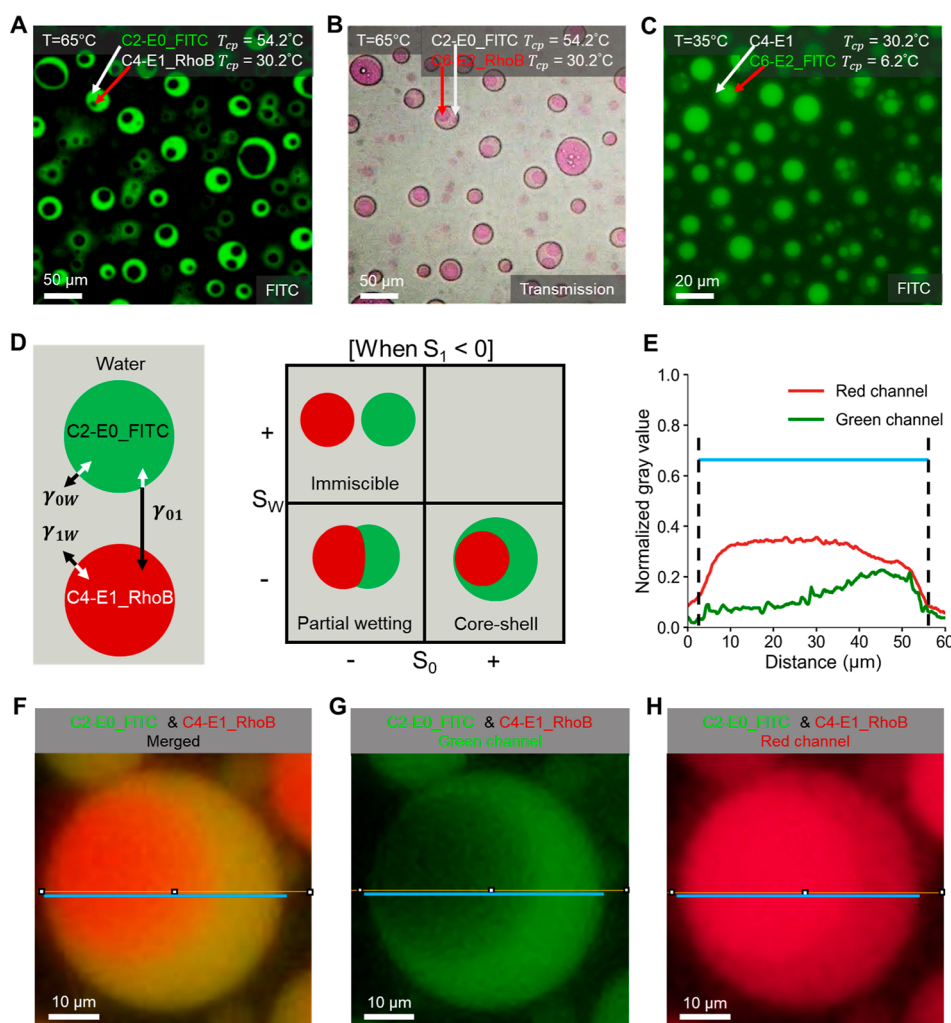
Figure 6. Microscopic images of multilayered coacervates formed by mixing two polymers with different LCSTs in water and heating the solution. Arrows indicate the dominant species in the core and shell structures. (A) C2−E0_FITC (shell, green) and C4−E1_RhoB (core, black) in the FITC channel at 65 °C. (B) C2−E0_FITC (shell, white) and C6−E2_RhoB (core, pink) in the bright-field channel at 65 °C. (C) C4−E1 (shell, black) and C6−E2_FITC (core, green) in the FITC channel at 65 °C. (D) Three possible morphologies of two immiscible droplets with water: immiscible, partial wetting, and core−shell. The γ_{ij}, γ_{jk}, and γ_{ik} are the interfacial tension between two liquid phases i and j, j and k, and i and k. The spreading coefficient (S_i), where $S_i = \gamma_{jk} - (\gamma_{ij} + \gamma_{ik})$, is determined for predicting the preferred morphology. Immiscible structure: $S_1 < 0$, $S_W > 0$, and $S_0 < 0$; partial wetting structure: $S_1 < 0$, $S_W < 0$, and $S_0 < 0$; and core−shell structure: $S_1 < 0$, $S_W < 0$, and $S_0 > 0$. (E−H) An example of multiphase coacervates (C2−E0_FITC and C4−E1_RhoB at 65 °C) for the calculation of the spreading coefficients and predicting the preferred morphology. (E) Fluorescence intensity profiles of green (C2−E0_FITC) and red (C4−E1_RhoB) channels along the yellow lines across the images in (F−H). Blue lines highlight the range of coacervates. Microscopic images of the coacervate are viewed in (F) merged green and red channels, (G) green channel, and (H) red channel.

the spreading coefficients of phases used for multiphasic coacervate formed from C4−E1 and C2−E0 (Figure 6E−H). As shown in the fluorescence intensity profile (Figure 6E) and images of coacervates at different channels (Figure 6F−H), red RhoB dye-conjugated C4−E1 was concentrated in the inner core, while green FITC fluorescence conjugated C2−E0 was mainly distributed in the outer shell. Here, C4−E1 (core, phase 1) in C2−E0 (shell, phase 0) was favored based on the experimental observation. The interfacial tension between each droplet (C4−E1 or C2−E0) and water (phase w) was evaluated as $\gamma_{1w} = 244$ μN/m and $\gamma_{0w} = 100$ μN/m, respectively, as calculated previously from the coalescence event (Figure 5C). The interfacial energy between C4−E1 droplet 1 and C2−E0 droplet 0 was also obtained as $\gamma_{01} = 16$ μN/m in a similar manner. The results of spreading coefficients are summarized in Table 2 as $S_1 = -160$ μN/m,

Table 2. Three Criteria of Spreading Coefficients for a Preferred C4−E1 in the C2−E0 Core−Shell Morphology

criteria of spreading coefficients for a phase 1 (C4−E1) in phase 0 (C2−E0) core−shell structure	calculated spreading coefficients[a]
$S_1 < 0$	$S_1 = \gamma_{0w} - (\gamma_{1w} + \gamma_{01})$ $= -160$ μN/m
$S_W < 0$	$S_W = \gamma_{01} - (\gamma_{0w} + \gamma_{1w})$ $= -328$ μN/m
$S_0 > 0$	$S_0 = \gamma_{1w} - (\gamma_{0w} + \gamma_{01})$ $= 128$ μN/m

[a]S_i and γ_{ij} represent the spreading coefficient of phase i and the interfacial tension between phase i and j, respectively. Subscript i and j can be 0 (coacervate phase of C2−E0), 1 (the coacervate phase of C4−E1), and w (dilute phase), respectively. Here, γ_{0w} (100 μN/m), γ_{1w} (244 μN/m), and γ_{01} (16 μN/m) are determined from the coalescence experiments.

$S_W = -328\ \mu\text{N/m}$, and $S_0 = 128\ \mu\text{N/m}$. These values meet the criteria of spreading coefficients (Figure 6D and Table 2) for the formation of a C4−E1 in C2−E0 core−shell structure, which is the same as experimental observations (Figure 6F). Note that we only observed core−shell structures in our experiments (Figure 6A−C).

■ CONCLUSIONS

In summary, using ROP of *N*-functional (1,4-oxazepan-7-one)s, we created a library of polyesteramides that show LCST-type, nonionic, single-component coacervation behavior in aqueous media. Above LCST, the water-tertiary amide bridging hydrogen bonds and hydrophobic interactions stabilize the coacervate. Interestingly, the phase-separated droplets show "liquid-like" behavior with low viscosity (0.1−10 Pa·s) and low interfacial tension (100−700 μN/m) that are comparable to intracellular biological coacervates. This liquid-like behavior originates from the hydration provided by tertiary amide−water hydrogen bonds above LCST which differentiate it from solid-like behavior of PNIPAM solutions.

Using tailored monomer chemistry and diverse polymerization techniques, we tuned the ratio between hydrophobic groups and HB sites with atom-level precision. With increasing hydrophobicity, the LCST of the resultant polymer shifted to a lower temperature, and the phase boundary was broadened. The increase in the ratio of hydrophobic to HB sites resulted in polymers with higher viscosities and interfacial tensions. By taking advantage of the differences in the mesoscopic properties of the coacervates formed from these polymers, we engineered multiphasic coacervates that resemble core−shell architectures commonly observed in intracellular biological coacervates such as nucleoli and stress granule-p-body complexes. In the future, the multiphasic structures formed from these synthetic nonionic polyesteramide coacervates are envisioned as a tool for investigating physicochemical principles deployed by living cells to spatiotemporally control the cargo partitioning, biochemical reaction rates, and intraorganellar signal transport.

■ ASSOCIATED CONTENT

Ⓢ Supporting Information

The Supporting Information is available free of charge at https://pubs.acs.org/doi/10.1021/jacs.3c06675.

>Experimental procedures, spectral data, additional images, computational data, and methods for all coacervate characterization (PDF)
>
>Coalescence of dense phase microdroplets for P$_{iBu}$ (MP4)
>
>Coalescence of dense phase microdroplets for P$_{EtOPr}$ (C4−E1) (MP4)
>
>Coalescence of dense phase microdroplets for C2−E0 (MP4)
>
>Coalescence of dense phase microdroplets for C6−E2 (MP4)

■ AUTHOR INFORMATION

Corresponding Author

Abraham Joy − *School of Polymer Science and Polymer Engineering, The University of Akron, Akron, Ohio 44325, United States;* ⓞ orcid.org/0000-0001-7781-3817; Email: abraham@uakron.edu

Authors

Xinhao Liu − *School of Polymer Science and Polymer Engineering, The University of Akron, Akron, Ohio 44325, United States;* ⓞ orcid.org/0000-0002-5640-1837

Abdol Hadi Mokarizadeh − *School of Polymer Science and Polymer Engineering, The University of Akron, Akron, Ohio 44325, United States;* ⓞ orcid.org/0000-0001-5922-7654

Amal Narayanan − *School of Polymer Science and Polymer Engineering, The University of Akron, Akron, Ohio 44325, United States;* ⓞ orcid.org/0000-0001-8159-6878

Prathamesh Mane − *School of Polymer Science and Polymer Engineering, The University of Akron, Akron, Ohio 44325, United States*

Avanti Pandit − *School of Polymer Science and Polymer Engineering, The University of Akron, Akron, Ohio 44325, United States*

Yen-Ming Tseng − *School of Polymer Science and Polymer Engineering, The University of Akron, Akron, Ohio 44325, United States;* ⓞ orcid.org/0000-0003-4531-9771

Mesfin Tsige − *School of Polymer Science and Polymer Engineering, The University of Akron, Akron, Ohio 44325, United States;* ⓞ orcid.org/0000-0002-7540-2050

Complete contact information is available at:
https://pubs.acs.org/10.1021/jacs.3c06675

Notes

The authors declare no competing financial interest.

■ ACKNOWLEDGMENTS

■ REFERENCES

(1) Crowe, C. D.; Keating, C. D. Liquid-Liquid Phase Separation in Artificial Cells. *Interface Focus* **2018**, *8* (5), 20180032.

(2) Choi, J. M.; Holehouse, A. S.; Pappu, R. V. Physical Principles Underlying the Complex Biology of Intracellular Phase Transitions. *Annu. Rev. Biophys.* **2020**, *49*, 107−133.

(3) Yewdall, N. A.; André, A. A.; Lu, T.; Spruijt, E. Coacervates as Models of Membraneless Organelles. *Curr. Opin. Colloid Interface Sci.* **2021**, *52*, 101416.

(4) Astoricchio, E.; Alfano, C.; Rajendran, L.; Temussi, P. A.; Pastore, A. The Wide World of Coacervates: From the Sea to Neurodegeneration. *Trends Biochem. Sci.* **2020**, *45* (8), 706−717.

(5) Taylor, S. W.; Waite, J. H. Marine Adhesives: From Molecular Dissection to Application. *Protein-Based Materials*; Birkhäuser Boston: Boston, MA, 1997; pp 217−248.

(6) Kim, S.; Huang, J.; Lee, Y.; Dutta, S.; Yoo, H. Y.; Jung, Y. M.; Jho, Y.; Zeng, H.; Hwang, D. S. Complexation and Coacervation of Like-Charged Polyelectrolytes Inspired by Mussels. *Proc. Natl. Acad. Sci. U.S.A.* **2016**, *113* (7), E847−E853.

(7) Yang, B.; Jin, S.; Park, Y.; Jung, Y. M.; Cha, H. J. Coacervation of Interfacial Adhesive Proteins for Initial Mussel Adhesion to a Wet Surface. *Small* **2018**, *14* (52), 1−12.

(8) Narayanan, A.; Menefee, J. R.; Liu, Q.; Dhinojwala, A.; Joy, A. Lower Critical Solution Temperature-Driven Self-Coacervation of Nonionic Polyester Underwater Adhesives. *ACS Nano* **2020**, *14* (7), 8359−8367.

(9) Alberti, S.; Gladfelter, A.; Mittag, T. Considerations and Challenges in Studying Liquid-Liquid Phase Separation and Biomolecular Condensates. *Cell* **2019**, *176* (3), 419−434.

(10) Perry, S. L.; Leon, L.; Hoffmann, K. Q.; Kade, M. J.; Priftis, D.; Black, K. A.; Wong, D.; Klein, R. A.; Pierce, C. F.; Margossian, K. O.; Whitmer, J. K.; Qin, J.; De Pablo, J. J.; Tirrell, M. Chirality-Selected

Phase Behaviour in Ionic Polypeptide Complexes. *Nat. Commun.* **2015**, *6*, 6052.

(11) Sing, C. E.; Perry, S. L. Recent Progress in the Science of Complex Coacervation. *Soft Matter* **2020**, *16* (12), 2885−2914.

(12) Onuchic, P. L.; Milin, A. N.; Alshareedah, I.; Deniz, A. A.; Banerjee, P. R. Divalent Cations Can Control a Switch-like Behavior in Heterotypic and Homotypic RNA Coacervates. *Sci. Rep.* **2019**, *9* (1), 12161.

(13) Quiroz, F. G.; Chilkoti, A. Sequence Heuristics to Encode Phase Behaviour in Intrinsically Disordered Protein Polymers. *Nat. Mater.* **2015**, *14* (11), 1164−1171.

(14) Banerjee, P. R.; Milin, A. N.; Moosa, M. M.; Onuchic, P. L.; Deniz, A. A. Reentrant Phase Transition Drives Dynamic Substructure Formation in Ribonucleoprotein Droplets. *Angew. Chem.* **2017**, *129* (38), 11512−11517.

(15) Spruijt, E.; Westphal, A. H.; Borst, J. W.; Cohen Stuart, M. A.; Van Der Gucht, J. Binodal Compositions of Polyelectrolyte Complexes. *Macromolecules* **2010**, *43* (15), 6476−6484.

(16) Abbas, M.; Lipiński, W. P.; Wang, J.; Spruijt, E. Peptide-Based Coacervates as Biomimetic Protocells. *Chem. Soc. Rev.* **2021**, *50*, 3690−3705.

(17) Lin, Y.; Fichou, Y.; Longhini, A. P.; Llanes, L. C.; Yin, P.; Bazan, G. C.; Kosik, K. S.; Han, S. Liquid-Liquid Phase Separation of Tau Driven by Hydrophobic Interaction Facilitates Fibrillization of Tau. *J. Mol. Biol.* **2021**, *433* (2), 166731.

(18) Tarakanova, A.; Yeo, G. C.; Baldock, C.; Weiss, A. S.; Buehler, M. J. Molecular Model of Human Tropoelastin and Implications of Associated Mutations. *Proc. Natl. Acad. Sci. U.S.A.* **2018**, *115* (28), 7338−7343.

(19) Li, P.; Banjade, S.; Cheng, H. C.; Kim, S.; Chen, B.; Guo, L.; Llaguno, M.; Hollingsworth, J. V.; King, D. S.; Banani, S. F.; Russo, P. S.; Jiang, Q. X.; Nixon, B. T.; Rosen, M. K. Phase Transitions in the Assembly of Multivalent Signalling Proteins. *Nature* **2012**, *483* (7389), 336−340.

(20) Bracha, D.; Walls, M. T.; Wei, M. T.; Zhu, L.; Kurian, M.; Avalos, J. L.; Toettcher, J. E.; Brangwynne, C. P. Mapping Local and Global Liquid Phase Behavior in Living Cells Using Photo-Oligomerizable Seeds. *Cell* **2018**, *175* (6), 1467−1480.e13.

(21) Shin, Y.; Chang, Y. C.; Lee, D. S. W.; Berry, J.; Sanders, D. W.; Ronceray, P.; Wingreen, N. S.; Haataja, M.; Brangwynne, C. P. Liquid Nuclear Condensates Mechanically Sense and Restructure the Genome. *Cell* **2018**, *175* (6), 1481−1491.e13.

(22) Aumiller, W. M.; Keating, C. D. Phosphorylation-Mediated RNA/Peptide Complex Coacervation as a Model for Intracellular Liquid Organelles. *Nat. Chem.* **2016**, *8* (2), 129−137.

(23) Boeynaems, S.; Bogaert, E.; Kovacs, D.; Konijnenberg, A.; Timmerman, E.; Volkov, A.; Guharoy, M.; De Decker, M.; Jaspers, T.; Ryan, V. H.; Janke, A. M.; Baatsen, P.; Vercruysse, T.; Kolaitis, R. M.; Daelemans, D.; Taylor, J. P.; Kedersha, N.; Anderson, P.; Impens, F.; Sobott, F.; Schymkowitz, J.; Rousseau, F.; Fawzi, N. L.; Robberecht, W.; Van Damme, P.; Tompa, P.; Van Den Bosch, L. Phase Separation of C9orf72 Dipeptide Repeats Perturbs Stress Granule Dynamics. *Mol. Cell* **2017**, *65* (6), 1044−1055.e5.

(24) Milin, A. N.; Deniz, A. A. Reentrant Phase Transitions and Non-Equilibrium Dynamics in Membraneless Organelles. *Biochemistry* **2018**, *57* (17), 2470−2477.

(25) Stewart, R. J.; Weaver, J. C.; Morse, D. E.; Waite, J. H. The Tube Cement of Phragmatopoma Californica: A Solid Foam. *J. Exp. Biol.* **2004**, *207* (26), 4727−4734.

(26) Neitzel, A. E.; De Hoe, G. X.; Tirrell, M. V. Expanding the Structural Diversity of Polyelectrolyte Complexes and Polyzwitterions. *Curr. Opin. Solid State Mater. Sci.* **2021**, *25* (2), 100897.

(27) Cruz, M. A.; Morris, D. L.; Swanson, J. P.; Kundu, M.; Mankoci, S. G.; Leeper, T. C.; Joy, A. Efficient Protein Encapsulation within Thermoresponsive Coacervate-Forming Biodegradable Polyesters. *ACS Macro Lett.* **2018**, *7* (4), 477−481.

(28) Swanson, J. P.; Monteleone, L. R.; Haso, F.; Costanzo, P. J.; Liu, T.; Joy, A. A Library of Thermoresponsive, Coacervate-Forming Biodegradable Polyesters. *Macromolecules* **2015**, *48* (12), 3834−3842.

(29) Swanson, J. P.; Cruz, M. A.; Monteleone, L. R.; Martinez, M. R.; Costanzo, P. J.; Joy, A. The Effect of Pendant Group Structure on the Thermoresponsive Properties of N-Substituted Polyesters. *Polym. Chem.* **2017**, *8* (46), 7195−7206.

(30) Wang, Q.; Schlenoff, J. B. The Polyelectrolyte Complex/Coacervate Continuum. *Macromolecules* **2014**, *47* (9), 3108−3116.

(31) Palmiero, U. C.; Paganini, C.; Kopp, M. R. G.; Linsenmeier, M.; Küffner, A. M.; Arosio, P. Programmable Zwitterionic Droplets as Biomolecular Sorters and Model of Membraneless Organelles. *Adv. Mater.* **2022**, *34* (4), 2104837.

(32) Wadsworth, G. M.; Zahurancik, W. J.; Zeng, X.; Pullara, P.; Lai, L. B.; Sidharthan, V.; Pappu, R. V.; Gopalan, V.; Banerjee, P. R. RNAs Undergo Phase Transitions with Lower Critical Solution Temperatures. *bioRxiv* **2022**, bioRxiv:2022.10.17.512593.

(33) Scott, W. A.; Gharakhanian, E. G.; Bell, A. G.; Evans, D.; Barun, E.; Houk, K. N.; Deming, T. J. Active Controlled and Tunable Coacervation Using Side-Chain Functional α-Helical Homopeptides. *J. Am. Chem. Soc.* **2021**, *143* (43), 18196−18203.

(34) Abbas, M.; Lipiński, W. P.; Nakashima, K. K.; Huck, W. T. S.; Spruijt, E. A Short Peptide Synthon for Liquid-Liquid Phase Separation. *Nat. Chem.* **2021**, *13* (11), 1046−1054.

(35) Swanson, J. P.; Martinez, M. R.; Cruz, M. A.; Mankoci, S. G.; Costanzo, P. J.; Joy, A. A Coacervate-Forming Biodegradable Polyester with Elevated LCST Based on Bis-(2-Methoxyethyl)Amine. *Polym. Chem.* **2016**, *7* (28), 4693−4702.

(36) Priftis, D.; Tirrell, M. Phase Behaviour and Complex Coacervation of Aqueous Polypeptide Solutions. *Soft Matter* **2012**, *8* (36), 9396−9405.

(37) Futscher, M. H.; Philipp, M.; Müller-Buschbaum, P.; Schulte, A. The Role of Backbone Hydration of Poly(N-Isopropyl Acrylamide) Across the Volume Phase Transition Compared to Its Monomer. *Sci. Rep.* **2017**, *7* (1), 17012.

(38) Li, T.; Tang, H.; Wu, P. Structural Investigation of Thermo-Responsive Poly(2-Isopropyl-2-Oxazoline) Hydrogel across the Volume Phase Transition. *Soft Matter* **2015**, *11* (10), 1911−1918.

(39) Wei, W.; Petrone, L.; Tan, Y.; Cai, H.; Israelachvili, J. N.; Miserez, A.; Waite, J. H. An Underwater Surface-Drying Peptide Inspired by a Mussel Adhesive Protein. *Adv. Funct. Mater.* **2016**, *26* (20), 3496−3507.

(40) Lau, H. K.; Li, L.; Jurusik, A. K.; Sabanayagam, C. R.; Kiick, K. L. Aqueous Liquid-Liquid Phase Separation of Resilin-Like Polypeptide/Polyethylene Glycol Solutions for the Formation of Microstructured Hydrogels. *ACS Biomater. Sci. Eng.* **2017**, *3* (5), 757−766.

(41) Filippov, A. D.; Sprakel, J.; Kamperman, M. Complex Coacervation and Metal-Ligand Bonding as Synergistic Design Elements for Aqueous Viscoelastic Materials. *Soft Matter* **2021**, *17* (12), 3294−3305.

(42) Huang, J.; Morin, F. J.; Laaser, J. E. Charge-Density-Dominated Phase Behavior and Viscoelasticity of Polyelectrolyte Complex Coacervates. *Macromolecules* **2019**, *52* (13), 4957−4967.

(43) Lu, T.; Spruijt, E. Multiphase Complex Coacervate Droplets. *J. Am. Chem. Soc.* **2020**, *142* (6), 2905−2914.

(44) Wang, X.; Zhang, Z.; Hadjichristidis, N. Poly(Amino Ester)s as an Emerging Synthetic Biodegradable Polymer Platform: Recent Developments and Future Trends. *Prog. Polym. Sci.* **2023**, *136*, 101634.

(45) Lau, K. H. A. Peptoids for Biomaterials Science. *Biomater. Sci.* **2014**, *2* (5), 627−633.

(46) Olivier, G. K.; Cho, A.; Sanii, B.; Connolly, M. D.; Tran, H.; Zuckermann, R. N. Antibody-Mimetic Peptoid Nanosheets for Molecular Recognition. *ACS Nano* **2013**, *7* (10), 9276−9286.

(47) Villuendas, I.; Molina, I.; Regaño, C.; Bueno, M.; Martínez de Ilarduya, A.; Galbis, J. A.; Muñoz-Guerra, S. Hydrolytic Degradation of Poly(Ester Amide)s Made from Tartaric and Succinic Acids: Influence of the Chemical Structure and Microstructure on Degradation Rate. *Macromolecules* **1999**, *32* (24), 8033−8040.

(48) Gokhale, S.; Xu, Y.; Joy, A. A Library of Multifunctional Polyesters with "Peptide-Like" Pendant Functional Groups. *Biomacromolecules* **2013**, *14* (8), 2489−2493.

(49) Verbraeken, B.; Monnery, B. D.; Lava, K.; Hoogenboom, R. The Chemistry of Poly(2-Oxazoline)S. *Eur. Polym. J.* **2017**, *88*, 451−469.

(50) Shyamroy, S.; Garnaik, B.; Sivaram, S. High Molecular Weight Poly(l-Lactic Acid)s by Polyesterification Using Diisopropylcarbodiimide (DIPC) and 4-(Dimethylamino) Pyridinium-p-Toluene Sulfonate (DPTS). *Polym. Bull.* **2015**, *72* (3), 405−415.

(51) Liu, X.; Jain, T.; Liu, Q.; Joy, A. Structural Insight into the Viscoelastic Behaviour of Elastomeric Polyesters: Effect of the Nature of Fatty Acid Side Chains and the Degree of Unsaturation. *Polym. Chem.* **2020**, *11* (32), 5216−5224.

(52) Wang, X.; Hadjichristidis, N. Organocatalytic Ring-Opening Polymerization of N-Acylated-1,4-Oxazepan-7-Ones Toward Well-Defined Poly(Ester Amide)s: Biodegradable Alternatives to Poly(2-Oxazoline)S. *ACS Macro Lett.* **2020**, *9* (4), 464−470.

(53) Xue, N.; Qiu, X. P.; Aseyev, V.; Winnik, F. M. Nonequilibrium Liquid-Liquid Phase Separation of Poly(N-Isopropylacrylamide) in Water/Methanol Mixtures. *Macromolecules* **2017**, *50* (11), 4446−4453.

(54) Zhou, D.; Pierucci, L.; Gao, Y.; O'Keeffe Ahern, J.; Huang, X.; Sigen, A.; Wang, W. Thermo- and PH-Responsive, Coacervate-Forming Hyperbranched Poly(β-Amino Ester)s for Selective Cell Binding. *ACS Appl. Mater. Interfaces* **2017**, *9* (7), 5793−5802.

(55) Diab, C.; Akiyama, Y.; Kataoka, K.; Winnik, F. M. Microcalorimetric Study of the Temperature-Induced Phase Separation in Aqueous Solutions of Poly(2-Isopropyl-2-Oxazolines). *Macromolecules* **2004**, *37* (7), 2556−2562.

(56) Lafontaine, D. L. J.; Riback, J. A.; Bascetin, R.; Brangwynne, C. P. The Nucleolus as a Multiphase Liquid Condensate. *Nat. Rev. Mol. Cell Biol.* **2021**, *22* (3), 165−182.

(57) Patel, A.; Lee, H. O. O.; Jawerth, L.; Maharana, S.; Jahnel, M.; Hein, M. Y. Y.; Stoynov, S.; Mahamid, J.; Saha, S.; Franzmann, T. M. M.; Pozniakovski, A.; Poser, I.; Maghelli, N.; Royer, L. A. A.; Weigert, M.; Myers, E. W. W.; Grill, S.; Drechsel, D.; Hyman, A. A. A.; Alberti, S. A Liquid-to-Solid Phase Transition of the ALS Protein FUS Accelerated by Disease Mutation. *Cell* **2015**, *162* (5), 1066−1077.

(58) Feric, M.; Vaidya, N.; Harmon, T. S.; Mitrea, D. M.; Zhu, L.; Richardson, T. M.; Kriwacki, R. W.; Pappu, R. V.; Brangwynne, C. P. Coexisting Liquid Phases Underlie Nucleolar Subcompartments. *Cell* **2016**, *165* (7), 1686−1697.

(59) Boeynaems, S.; Alberti, S.; Fawzi, N. L.; Mittag, T.; Polymenidou, M.; Rousseau, F.; Schymkowitz, J.; Shorter, J.; Wolozin, B.; Van Den Bosch, L.; Tompa, P.; Fuxreiter, M. Protein Phase Separation: A New Phase in Cell Biology. *Trends Cell Biol.* **2018**, *28* (6), 420−435.

(60) Iglesias-Artola, J. M.; Drobot, B.; Kar, M.; Fritsch, A. W.; Mutschler, H.; Dora Tang, T. Y.; Kreysing, M. Charge-Density Reduction Promotes Ribozyme Activity in RNA-Peptide Coacervates via RNA Fluidization and Magnesium Partitioning. *Nat. Chem.* **2022**, *14* (4), 407−416.

(61) Meyer, D. E.; Chilkoti, A. Quantification of the Effects of Chain Length and Concentration on the Thermal Behavior of Elastin-like Polypeptides. *Biomacromolecules* **2004**, *5* (3), 846−851.

(62) Brennan, M. J.; Kilbride, B. F.; Wilker, J. J.; Liu, J. C. A Bioinspired Elastin-Based Protein for a Cytocompatible Underwater Adhesive. *Biomaterials* **2017**, *124*, 116−125.

(63) Madinya, J. J.; Chang, L. W.; Perry, S. L.; Sing, C. E. Sequence-Dependent Self-Coacervation in High Charge-Density Polyampholytes. *Mol. Syst. Des. Eng.* **2020**, *5* (3), 632−644.

(64) Yang, H.; Yang, S.; Kong, J.; Dong, A.; Yu, S. Obtaining Information about Protein Secondary Structures in Aqueous Solution Using Fourier Transform IR Spectroscopy. *Nat. Protoc.* **2015**, *10* (3), 382−396.

(65) Li, T.; Tang, H.; Wu, P. Molecular Evolution of Poly(2-Isopropyl-2-Oxazoline) Aqueous Solution during the Liquid-Liquid Phase Separation and Phase Transition Process. *Langmuir* **2015**, *31* (24), 6870−6878.

(66) Sun, B.; Lin, Y.; Wu, P.; Siesler, H. W. A FTIR and 2D-IR Spectroscopic Study on the Microdynamics Phase Separation Mechanism of the Poly(N-Isopropylacrylamide) Aqueous Solution. *Macromolecules* **2008**, *41* (4), 1512−1520.

(67) Okada, Y.; Tanaka, F. Cooperative Hydration, Chain Collapse, and Flat LCST Behavior in Aqueous Poly(N-Isopropylacrylamide) Solutions. *Macromolecules* **2005**, *38* (10), 4465−4471.

(68) Dormidontova, E. E. Role of Competitive PEO-Water and Water-Water Hydrogen Bonding in Aqueous Solution PEO Behavior. *Macromolecules* **2002**, *35* (3), 987−1001.

(69) Simon, J. R.; Carroll, N. J.; Rubinstein, M.; Chilkoti, A.; López, G. P. Programming Molecular Self-Assembly of Intrinsically Disordered Proteins Containing Sequences of Low Complexity. *Nat. Chem.* **2017**, *9* (6), 509−515.

(70) Lou, J.; Friedowitz, S.; Qin, J.; Xia, Y. Tunable Coacervation of Well-Defined Homologous Polyanions and Polycations by Local Polarity. *ACS Cent. Sci.* **2019**, *5* (3), 549−557.

(71) Lu, T.; Nakashima, K. K.; Spruijt, E. Temperature-Responsive Peptide-Nucleotide Coacervates. *J. Phys. Chem. B* **2021**, *125* (12), 3080−3091.

(72) Munder, M. C.; Midtvedt, D.; Franzmann, T.; Nüske, E.; Otto, O.; Herbig, M.; Ulbricht, E.; Müller, P.; Taubenberger, A.; Maharana, S.; Malinovska, L.; Richter, D.; Guck, J.; Zaburdaev, V.; Alberti, S. A PH-Driven Transition of the Cytoplasm from a Fluid- to a Solid-like State Promotes Entry into Dormancy. *Elife* **2016**, *5* (MARCH2016), No. e09347.

(73) Wei, M. T.; Elbaum-Garfinkle, S.; Holehouse, A. S.; Chen, C. C. H.; Feric, M.; Arnold, C. B.; Priestley, R. D.; Pappu, R. V.; Brangwynne, C. P. Phase Behaviour of Disordered Proteins Underlying Low Density and High Permeability of Liquid Organelles. *Nat. Chem.* **2017**, *9* (11), 1118−1125.

(74) Elbaum-Garfinkle, S.; Kim, Y.; Szczepaniak, K.; Chen, C. C. H.; Eckmann, C. R.; Myong, S.; Brangwynne, C. P. The Disordered P Granule Protein LAF-1 Drives Phase Separation into Droplets with Tunable Viscosity and Dynamics. *Proc. Natl. Acad. Sci. U.S.A.* **2015**, *112* (23), 7189−7194.

(75) Wang, H.; Kelley, F.; Hoffmann, C.; Milovanovic, D.; Schuster, B. S.; Shi, Z. Quantifying the Material Properties of Protein Condensates through Micropipette Aspiration. *Biophys. J.* **2022**, *121* (3), 308a.

(76) Park, S.; Barnes, R.; Lin, Y.; Jeon, B. J.; Najafi, S.; Delaney, K. T.; Fredrickson, G. H.; Shea, J. E.; Hwang, D. S.; Han, S. Dehydration Entropy Drives Liquid-Liquid Phase Separation by Molecular Crowding. *Commun. Chem.* **2020**, *3* (1), 83.

(77) Gucht, J. v. d.; Spruijt, E.; Lemmers, M.; Cohen Stuart, M. A. Polyelectrolyte Complexes: Bulk Phases and Colloidal Systems. *J. Colloid Interface Sci.* **2011**, *361* (2), 407−422.

(78) Mohammadi, P.; Beaune, G.; Stokke, B. T.; Timonen, J. V. I.; Linder, M. B. Self-Coacervation of a Silk-Like Protein and Its Use As an Adhesive for Cellulosic Materials. *ACS Macro Lett.* **2018**, *7* (9), 1120−1125.

(79) Jho, Y. S.; Yoo, H. Y.; Lin, Y.; Han, S.; Hwang, D. S. Molecular and Structural Basis of Low Interfacial Energy of Complex Coacervates in Water. *Adv. Colloid Interface Sci.* **2017**, *239*, 61−73.

(80) Brangwynne, C. P.; Eckmann, C. R.; Courson, D. S.; Rybarska, A.; Hoege, C.; Gharakhani, J.; Jülicher, F.; Hyman, A. A. Germline P Granules Are Liquid Droplets That Localize by Controlled Dissolution/Condensation. *Science* **2009**, *324* (5935), 1729−1732.

(81) Sanders, D. W.; Kedersha, N.; Lee, D. S. W.; Strom, A. R.; Drake, V.; Riback, J. A.; Bracha, D.; Eeftens, J. M.; Iwanicki, A.; Wang, A.; Wei, M. T.; Whitney, G.; Lyons, S. M.; Anderson, P.; Jacobs, W. M.; Ivanov, P.; Brangwynne, C. P. Competing Protein-RNA Interaction Networks Control Multiphase Intracellular Organization. *Cell* **2020**, *181* (2), 306−324.e28.

(82) Nakagawa, S.; Yamazaki, T.; Hirose, T. Molecular Dissection of Nuclear Paraspeckles: Towards Understanding the Emerging World of the RNP Milieu. *Open Biol.* **2018**, *8* (10), 180150.

(83) Riback, J. A.; Zhu, L.; Ferrolino, M. C.; Tolbert, M.; Mitrea, D. M.; Sanders, D. W.; Wei, M. T.; Kriwacki, R. W.; Brangwynne, C. P. Composition-Dependent Thermodynamics of Intracellular Phase Separation. *Nature* **2020**, *581* (7807), 209−214.

(84) Mason, A. F.; Buddingh, B. C.; Williams, D. S.; Van Hest, J. C. M. Hierarchical Self-Assembly of a Copolymer-Stabilized Coacervate Protocell. *J. Am. Chem. Soc.* **2017**, *139* (48), 17309−17312.

(85) Mountain, G. A.; Keating, C. D. Formation of Multiphase Complex Coacervates and Partitioning of Biomolecules within Them. *Biomacromolecules* **2020**, *21* (2), 630−640.

(86) Erkamp, N. A.; Sneideris, T.; Ausserwöger, H.; Qian, D.; Qamar, S.; Nixon-Abell, J.; St George-Hyslop, P.; Schmit, J. D.; Weitz, D. A.; Knowles, T. P. J. Spatially Non-Uniform Condensates Emerge from Dynamically Arrested Phase Separation. *Nat. Commun.* **2023**, *14* (1), 684.

(87) Matsumoto, M.; Asoh, T.; Shoji, T.; Tsuboi, Y. Formation of Single Double-Layered Coacervate of Poly(N,N-Diethylacrylamide) in Water by a Laser Tweezer. *Langmuir* **2021**, *37* (9), 2874−2883.

(88) Fisher, R. S.; Elbaum-Garfinkle, S. Tunable Multiphase Dynamics of Arginine and Lysine Liquid Condensates. *Nat. Commun.* **2020**, *11* (1), 4628.

(89) Seo, K. D.; Shin, S.; Yoo, H. Y.; Cao, J.; Lee, S.; Yoo, J. W.; Kim, D. S.; Hwang, D. S. Stabilizing Coacervate by Microfluidic Engulfment Induced by Controlled Interfacial Energy. *Biomacromolecules* **2020**, *21* (2), 930−938.